JOURNAL OF THERMOPHYSICS AND HEAT TRANSFER
Vol. 14, No. 3, July–September 2000

Ablation Onset in Unsteady Hypersonic Flow About Nose Tip with Cavity

Sidra I. Silton* and David B. Goldstein†
University of Texas at Austin, Austin, Texas 78712-1085

A forward-facing cavity is examined as a means of reducing the severe heating and ablation at the nose tip of a hypersonic vehicle. Whereas previous studies have concentrated on heating rates alone, the present study addresses the effects of the cavity on ablation onset times through experiments and joined flowfield/heat conduction simulations. A viable experimental technique has been developed to study ablation in the Mach 5 wind tunnel at the University of Texas at Austin J.J. Pickle Research Center. Using this technique, the time to ablation onset for a nonoptimized, rounded-lip, deep-cavity model has been found to be similar to that of the baseline hemisphere–cylinder model. Additionally, the computational technique predicts ablation onset times that agree surprisingly well with the Mach 5 experimental data. Thus, a benchmark is achieved in the computational techniques for future use for determining the experimental flowfield physics of this complex, unsteady hypersonic flow problem.

Nomenclature

D = cavity diameter, cm
D_n = nose diameter, cm
dt_i = initial time step in heat conduction calculations, s
$dx_{\min}$ = computational surface cell thickness, cm
h = heat conduction coefficient, W/m^{2}K
k = thermal conductivity, W/mK
L = cavity depth, measured from the cavity lip to the cavity base, cm
L/D = length-to-diameter ratio of cavity
q = surface heat flux, W/m^2
T = temperature, K
T_{aw} = adiabatic wall temperature, K
T_{stag} = wind-tunnel stagnation temperature, K
T_w = wall temperature, K
t = time, s
t_{final} = final clock time for heat conduction solution, s
x, X = horizontal position, m
y, Y = vertical position, m
θ = angle off of centerline of model, deg
μ = viscosity, Ns/m^2

Introduction

HYPERSONIC vehicles are exposed to severe heating, and shape changes due to material ablation may occur. These shape changes need to be minimized when they produce unacceptable perturbations in the aerodynamics and, therefore, the vehicle flight path. The heat loads and material ablation that lead to the shape changes are most critical at the nose tip. Thus, it is desirable to find ways to delay ablation onset, decrease the rate of ablation, or devise a way to ensure ablation is uniform. In the present study, the delay of ablation onset is the primary goal and is of particular importance for vehicles having extremely short flight times.

The introduction of a forward-facing cavity into the nose tip of a hypersonic projectile (Fig. 1) has recently been found to reduce local heating over the entire nose region compared to that of a similar spherical nose tip.[1,2] A range of cavity geometries that are effective in decreasing the heating rate has been explored. In these studies, however, the effects of the cavity on ablation itself have not been directly addressed.

Preliminary experiments using an infrared camera[3] indicated that large-diameter, shallow cavities (L/D between 0.15 and 0.35) created a stable cool ring just outside of a sharp cavity lip, with temperatures locally lower than those found on a simple spherical nose. A joint numerical and experimental study[4] concluded that sharp cavity lips produce not only a separated recirculation region (accounting for the cool ring) but also severe heating just inside the cavity for weakly oscillating flows. In time-accurate numerical simulations,[5] resonant oscillations were obtained if either freestream fluctuations were present or a sufficiently deep cavity was employed. Yuceil[2] experimentally found substantial cooling over the entire nose region for a cavity of $L/D = 2.0$, compared with the case with no cavity. Engblom and Goldstein[6] numerically showed that the local heat flux everywhere on the surface was reduced when strong longitudinal pressure oscillations within the cavity induced large bow shock oscillations. That numerical effort also found that the heat reduction benefit appeared to increase with mean relative bow shock speed. The reader is specifically referred to the paper by Engblom and Goldstein[6] for a detailed discussion of the heat flux reduction mechanisms.

The present paper presents a portion of the results from a joint numerical/experimental study on the effects of a forward-facing cavity on the ablation of a nose tip in hypersonic flow. This study has four objectives: 1) to develop a viable experimental technique for studying ablation in the University of Texas at Austin J.J. Pickle Research Center (PRC) Wind Tunnel Laboratory, because the facility is not a high-enthalpy tunnel; 2) to validate the further use of the computational model for the determination of ablation onset time; 3) to attempt to confirm, numerically and/or experimentally, that the introduction of a forward-facing cavity into a hypersonic projectile delays ablation onset in the nose region; and 4) to optimize the cavity configuration for the greatest delay of ablation onset. The current paper addresses the first two objectives. As will be seen, considerable care has been taken to establish the adequacy of the computations. The third and fourth objectives are currently being pursued.

Experimental Methodology

Wind Tunnel

All experiments were conducted in the Mach 5 blowdown wind tunnel at PRC. The wind tunnel had a rectangular test section 15.24 cm wide, 17.78 cm high, and 68.58 cm long. A floor slot was

---

Presented as Paper 98-0169 at the AIAA 36th Aerospace Sciences Meeting, Reno, NV, 12–15 January 1998; received 26 July 1999; presented as Paper 2000-0203 at the AIAA 38th Aerospace Sciences Meeting, Reno, NV, 10–13 January 2000; revision received 18 February 2000; accepted for publication 25 February 2000.

*Graduate Research Assistant, Center for Aeromechanics Research, Department of Aerospace Engineering and Engineering Mechanics. Student Member AIAA.

†Associate Professor, Center for Aeromechanics Research, Department of Aerospace Engineering and Engineering Mechanics. Senior Member AIAA.

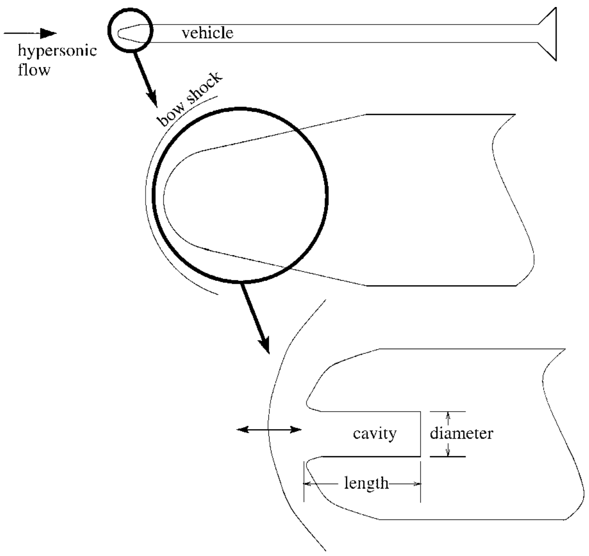

Fig. 1 Schematic of axial forward-facing cavity in the nose region of a hypersonic vehicle.

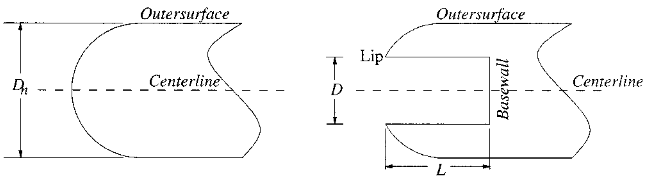

Hemisphere-cylinder (baseline) **Axial Cavity—Infinitely Sharp Lip**

Fig. 2 Nose-cavity geometries used in numerical simulations (rounded-lip geometry not shown).

used to mount the models, and circular side-wall windows allowed for video imaging. Compressed air (stored at 17.24 MPa in four external tanks with a total volume of 3.964 m^3) allowed for run times of up to 1 min without a significant drop in the tunnel stagnation pressure. The incoming air was heated by two banks of nichrome wire resistive heaters (420 kW each) located upstream of the stagnation chamber.

The tunnel was operated at a nominal stagnation pressure and temperature of 2.30 MPa and 370 K, respectively. At the freestream Mach number of 4.92, these stagnation conditions correspond to a freestream unit Reynolds number of 5.0×10^5 cm^{-1} and a freestream velocity, static air pressure, and static temperature of 787 m/s, 4694 Pa, and 64 K, respectively.

Models

A missile nose is typically a blunted cone–cylinder configuration (Fig. 1). However, because the focus of this work was on the stagnation region, the missile nose was modeled as a sphere–cylinder as in previous work.[1,2,7] Therefore, the basic model geometry was a hemispherically blunted cylinder with a streamwise circular nose cavity (Fig. 2).

The material chosen for the model needed to ablate at low temperatures because T_{stag} was considerably lower than that in actual flight. Water ice was chosen as a suitable material because it is inexpensive, well characterized, and neither toxic, flammable, nor corrosive. Ice also has a very low sublimation rate (low vapor pressure) at low temperatures. Ice has a melting or (in this case) ablation temperature of 273 K, nearly 100 K below T_{stag}. To delay the onset of ablation for several seconds into the tunnel run and to establish a known, uniform initial temperature, the ice was initially cooled to the boiling point of liquid nitrogen (LN2), 78 K.

Several models were used over the course of the study. Each ice model was frozen in a polished aluminum mold (Fig. 3b). The mold created a model with $D_n = 2.54$ cm. Different cavity lengths L were

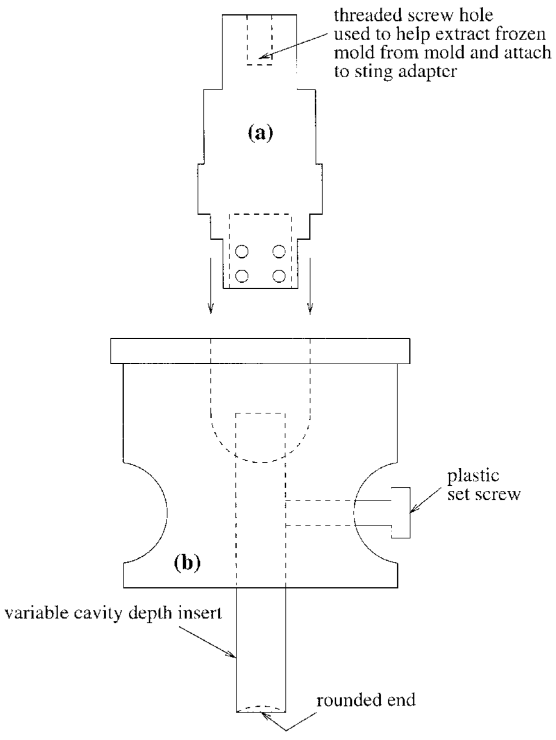

Fig. 3 Apparatus used to create ice models for experiment: a) spindle and b) mold.

obtained by fixing an insert in the mold at the required location prior to the freezing process. One end of the insert had a 1.27-cm radius of curvature, equal to that of the nose, which ensured that a spherical nose was obtained for the baseline case, that is, $L = 0$. The other end of the insert had a flat bottom to produce a flat bottom cavity when cavity depths greater than zero were desired. A cavity diameter of one-half the model nose diameter ($D = 1.27$ cm) was chosen for consistency with previous work.[1,2]

The mold, lightly coated with Pam vegetable oil spray to assist in the removal of the ice, was filled with distilled water. Fiberglass threads were added to strengthen the model. Without the addition of the fiberglass, the ice shattered during tunnel startup. The mass of fiberglass added (≈ 0.1 g) was not a significant fraction of the total mass of the ice. The fiberglass was not believed to have changed the thermal characteristics of the ice but instead produced a tough, viable, and fiber-reinforced composite.

After the fiberglass was mixed into the water, a brass spindle (Fig. 3a) was placed in the mold (Fig. 3b). The spindle was the base on which the model was attached to the sting adapter (and sting) (Fig. 4, as indicated). Holes were drilled into the cup (the portion of the spindle around which the ice was formed) so that water would be present on both the interior and the exterior of the cup. The entire mold was then placed in LN2 vapors (a few inches above a pool of LN2) for approximately 20 min until the water was completely frozen. The spindle, with the ice model attached, was then forcibly pulled free of the mold. For rounded-lip models (see Experimental Results), the ice cavity lip was smoothed with sandpaper to approximately the desired radius. This was accomplished with the frozen spindle either held by hand or turned in a drill press. The spindle, with the completed ice model attached, was then placed back in the LN2 vapors for 1–2 additional hours to reduce the temperature of the ice gradually to 78 K.

Model Shielding

Shielding of the model was required in the present study to protect the model from irregular heating during startup of the wind tunnel. The shield consisted of two parts, one reusable (outer shroud) and the other expendable (shroud cap) (Fig. 4, as indicated). The shield was assumed to provide sufficient insulation of the model from the

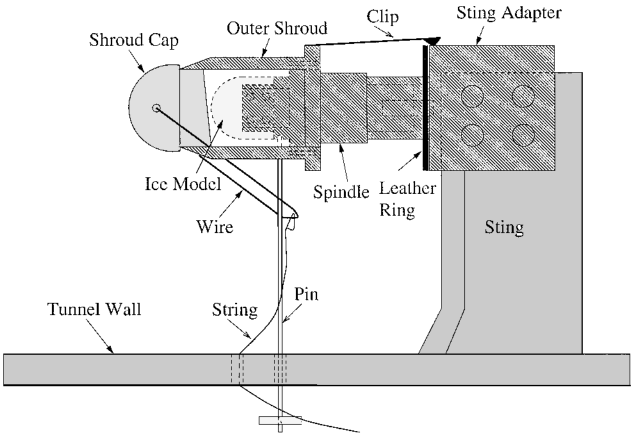

Fig. 4 Schematic representation of wind-tunnel-mounted model during tunnel startup while ice is protected.

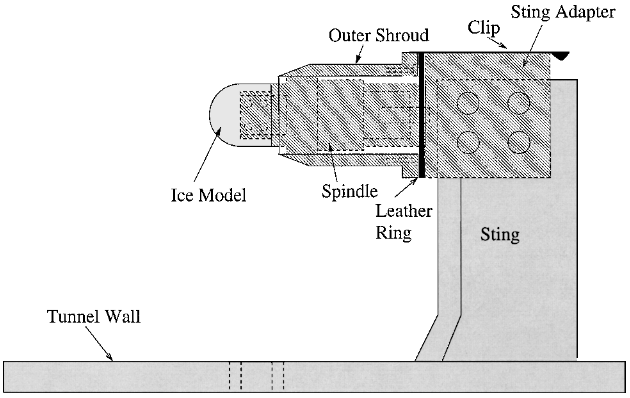

Fig. 5 Schematic of exposed wind-tunnel model after tunnel startup is complete.

flowfield because there was no direct contact between the shield and the ice. However, tests have not yet been conducted to determine the temperature rise in the nose during startup.

The outer shroud, which fit over the spindle, consisted of a hollow brass cylinder with a brass flange attached to one end. Brass was chosen for the shielding to match the thermal expansion of the spindle (thereby reducing the possibility of the shield sticking to the spindle). The outer shroud was kept in place with a long threaded pin that went through the shroud and into a threaded hole in the spindle. The outer shroud was designed such that aerodynamic forces would push it back over the spindle after the pin was removed. A spring metal clip kept the retracted outer shroud in place for the remainder of the run. The shroud cap was a pine wood plug that fit into the outer shroud to cover the ice.

Experimental Procedure

Before each run, the interior of the outer shroud was coated with graphite powder as a dry lubricant. The outer shroud was then placed in LN2 to cool independently before it was positioned over the ice model and spindle (also coated with graphite powder). The entire assembly (outer shroud and model) was then placed back in the LN2 to ensure an uniform temperature. The cooled assembly was then screwed into the sting adapter, the shroud cap positioned, and the pin fitted into place (Fig. 4). To minimize heating of the spindle during this time and to prevent the accumulation of frost, the sting adapter was precooled with LN2, the back flow into the tunnel was blocked with paper, and the air conditioning was used to dehumidify the room.

Once conditions in the wind tunnel stabilized after startup (15–20 s into the run), the pin holding the shield in place was removed, which allowed the outer shroud to slide back over the spindle. The shroud cap then came loose and flew off downstream, thereby exposing the ice model (Fig. 5). The time at which the ice became exposed to freestream conditions was considered time zero, although images were taken prior to this time.

Video Imaging Process

A Panasonic WV-3250 video camera with horizontal resolution of 350 lines at center imaged the run at 30 Hz. The timer on the video camera was utilized to determine at what time the shield was removed, how long after this time ablation began to occur, and how quickly the material ablated. The video camera was set perpendicular to the circular viewing window, and so little of the cavity interior could be visualized.

The video images were digitized and extracted at 1-s intervals during postprocessing. For each such still image, the pixel location of the most forward position of the model could be determined. A least-squares-fit line was calculated and the slope determined the recession rate for that run. By extending the line back to a zero change in position, a more exact ablation onset time was determined.

Numerical Methodology

Computer Code Description

The commercial computer code, INCA Version 2.5 (Ref. 8) (licensed from Amtec Engineering), was used for the fluid dynamics (flowfield) portion of this study (also used in Refs. 1, 4, and 5). INCA is a finite volume code that utilizes flux splitting with upwinding to capture strong shocks. Fluxes are computed with the flux splitting of Steger and Warming.[9] INCA offers an efficient lower-upper successive Gauss–Seidel (LU-SGS) implicit solver to calculate steady flowfields. The LU-SGS algorithm approximately solves the system of equations using two sweeps of a point Gauss–Seidel relaxation. A variation of the LU-SGS implicit solver to calculate unsteady flows, available within INCA, was utilized in the present work. This second-order accurate algorithm permitted much larger time steps than a simple Euler step method by performing a sufficient number of subiterations at each time step.

A finite element computer program for nonlinear heat conduction problems, COYOTE Version 2.5 (Ref. 10) (obtained form Sandia National Laboratories), was used to solve the solid body heat conduction portion of the problem. COYOTE uses the Adams–Bashforth predictor to obtain an implicit integration method that is second-order accurate in time. This predictor/corrector algorithm allowed the time step to be selected dynamically based on a user specified truncation error tolerance.

Algebraic grids were created for the external fluid domain using GRIDALL[11] (Amtec Engineering), whereas unstructured grids were created for the solid body using FASTQ[12] (Sandia National Laboratories).

Numerical Assumptions

Body geometry, material properties, and freestream conditions were consistent with those of the experiments described earlier. However, the computational verification was performed for only three body geometries: a simple hemisphere–cylinder baseline case, an infinitely sharp-lip cavity case, and a rounded-lip (1.0 mm) cavity case. For both cavity cases, L was 2.54 cm. To solve the numerical problem within a reasonable time period, a number of simplifying assumptions were made in both the flowfield and solid body heat conduction calculations.

First, the flowfield calculation assumed axisymmetric flow of a thermally and calorically perfect gas. Axisymmetry was appropriate because the bow shock had previously been found to oscillate axisymmetrically in front of deep cavities,[2] and pressure oscillations at the cavity basewall have been found to be planar.[2,4,13] Additionally, the wall temperature boundary condition was assumed to be 100 K (instead of 78 K, the boiling point of LN2) to allow for a possible small increase in the surface temperature of the model during final model preparation and wind-tunnel startup. Finally, the flow was assumed to be laminar because there is no clear indication (either experimentally or computationally) as to when, or if, the flow became turbulent. Specifically, boundary-layer transition was not expected in the small stagnation region at the cavity lip due to low-speed flow and the favorable pressure gradient present in this region during the inflow portion of the pressure oscillation cycle. If the flow were to become turbulent, heating would be most critical in the vicinity of the cavity lip. As this laminar flow assumption is somewhat in doubt, the use of a k–ε turbulence model was investigated (see following) to determine whether a laminar or turbulent flow assumption showed better agreement with the experimental results.

For the solid-body heat conduction calculations, the entire body was assumed to be 100 K initially. In addition, the thermal properties of the body were assumed to be only those of water ice and did not take into account the presence of other materials in the experiment. Variable material properties were utilized for density,[14] specific heat,[15] and thermal conductivity.[16] Density, specific heat, and thermal conductivity range from 934 kg/m^3, 882 J/kgK, and 6.5 W/mK, respectively, at 100 K to 910 kg/m^3, 2100 J/kgK, and 2.2 W/mK, respectively, at 273 K.

Numerical Procedure

Because of much shorter characteristic times in the oscillating flowfield [$\mathcal{O}(1/3000\ \mathrm{s})$] than in the solid body [$\mathcal{O}(1\ \mathrm{s})$], it was not practical to try to solve the two parts of the problem in a fully coupled manner as a few seconds were required for the solid body to begin to ablate (melt). For this reason, the linking procedure, discussed hereafter, was developed. Because the baseline case had a steady flowfield and the cavity case had an oscillatory flowfield, the flowfield procedures are discussed separately.

Baseline Procedure

The output files from the steady baseline hemisphere–cylinder flowfield solution were used to obtain $q(x, y)$ over the solid-body surface. This heat flux distribution was then used to calculate $h(x, y)$ from

$$h(x, y) = \frac{q(x, y)}{T_w - T_{\mathrm{aw}}(x, y)} \tag{1}$$

$T_{\mathrm{aw}}(x, y)$ was obtained via a separate flowfield calculation under the assumption of an adiabatic wall boundary condition. These data were input as boundary conditions into the heat conduction code until the stagnation point (the point of highest heating) reached its melting point.

Cavity Procedure

When an axial cavity, 2.54 cm in diameter and 5.08 cm in length ($L/D = 2.0$) or deeper, was introduced into a $D_n = 5.08$ cm nose tip of a projectile at Mach 5, the bow shock oscillations were self-sustaining.[1] Therefore, the flowfield must be numerically solved in a time-accurate manner.

The restart file from a coarse-grid, pseudosteady flowfield solution (having constant amplitude basewall pressure oscillations) was utilized to generate a time-accurate solution of the flowfield and the corresponding surface heat flux distribution. The solution was then interpolated to a finer grid and run further in time. Generally, 1 pressure oscillation cycle was solved using approximately 4000 global time steps and 6 subiterations per time step. The computational time requirement (at the converged spatial resolution) was typically 4 CPU h/cycle on a Cray T90. The solution was assumed converged once the time-averaged (mean) surface heat flux distribution did not change appreciably from one cycle to the next. The mean surface heat flux distribution was obtained by averaging the instantaneous surface heat fluxes over one complete cycle.[1]

The converged mean surface heat flux distribution was used to obtain $h(x, y)$ [Eq. (1)]. $T_{\mathrm{aw}}(x, y)$ was obtained by averaging the instantaneous wall temperature over one complete cycle where the time-accurate flowfield solution was computed assuming an adiabatic wall boundary condition in a separate simulation. These data were input as boundary conditions into the heat conduction code until some point reached its melting temperature.

Heat Conduction Code Procedure

$T_{\mathrm{aw}}(x, y)$ and $h(x, y)$, obtained from the flow solver, as described earlier, were used as boundary condition input for the heat conduction code. The heat conduction code was then run from time $t = 0$ s. The baseline case used an initial time step $\mathrm{d}t_i$ of 0.02 s (determined based on local Fourier and Biot numbers), which COYOTE then varied dynamically based on an integration tolerance criteria of 1.0×10^{-4}. The baseline solution, obtained up to $t_{\mathrm{final}} = 5$ s, typically required 1.5 h of CPU time on a single processor of a smaller Cray SV1. For the sharp-lip cavity case, $\mathrm{d}t_i = 0.01$ s was utilized due to finer grid resolution. The solution, obtained to $t_{\mathrm{final}} = 3$ s, typically required 2 h of CPU time on the Cray SV1 due to an overresolved grid. For the rounded-lip cavity case, $\mathrm{d}t_i = 0.02$ s was utilized, and the solution, obtained to $t_{\mathrm{final}} = 4$ s, typically required 1.5 h of CPU time on a smaller Cray J90 due to a better constructed, though still overresolved, grid.

Grid Resolution

A grid resolution study was conducted for the flowfield computations for all three cases to determine the maximum tolerable surface cell thickness. A grid resolution study for the solid-body heat conduction computation was carried out only for the baseline case. Details of the grid resolution studies can be found in the Numerical Results subsection.

Results

The experimental and numerical results are presented separately hereafter. Each section is subdivided into the specific geometrical cases that were investigated.

Experimental Results

This study was limited to investigating the effects of L/D and the cavity lip radius on the onset time of and the rate of ablation. Other parameters that may have influenced the results (including the ratio of D to D_n, cavity base shape, and Reynolds number) have previously been examined[1,2] in relation to their effect on surface heating, but not ablation.

Much of the present study focused on the baseline case and a deep-cavity geometry ($L/D = 2.0$) that was found to self-sustain bow shock oscillations[1] and that had a great effect on surface heating.[1,2] Three shallower cavities ($L/D =$ 0.25, 0.5, and 1.0), which were found to have cool recirculation regions at the nose tip,[4] were also examined, though in less detail. The present experimental findings will be separated into three sections: baseline model, deep-cavity models, and shallow-cavity models. A synthesis of the findings is also presented.

Baseline Model

Three separate wind-tunnel runs were conducted for the baseline model to assess the repeatability of the results. It was found in all three that the stagnation point may not be the first point to begin melting. The sides of the model (near $\theta \sim 45$ deg) may melt first and/or more quickly, as a cusped shape begins to form. This phenomenon is quite noticeable from viewing the time-lapse photographs (Figs. 6a–6f). The cusped shape phenomenon was also seen by Reinecke and Guillot[17] in their numerical ablation and shape change calculations and by Reinecke and Sherman[18] in their arc jet experiments. As in those studies, the shape change was caused by boundary-layer transition near the sonic point. The heat transfer below a turbulent boundary layer is very large, larger than at the stagnation point. Therefore, the material will first ablate near the boundary-layer transition point. In the present experiments, small protruding glass fibers, natural transition, a noisy freestream, or model irregularities may have aided natural boundary-layer transition. The presence of this classical laminar/turbulent shape (Fig. 6f) supports the use of ice in the wind tunnel to simulate nose-tip ablation.

The recession of the stagnation point over time is seen in Fig. 7, in which symbols with no lines are for times prior to the presumed onset of abation, and lines are least-square linear fits of the data

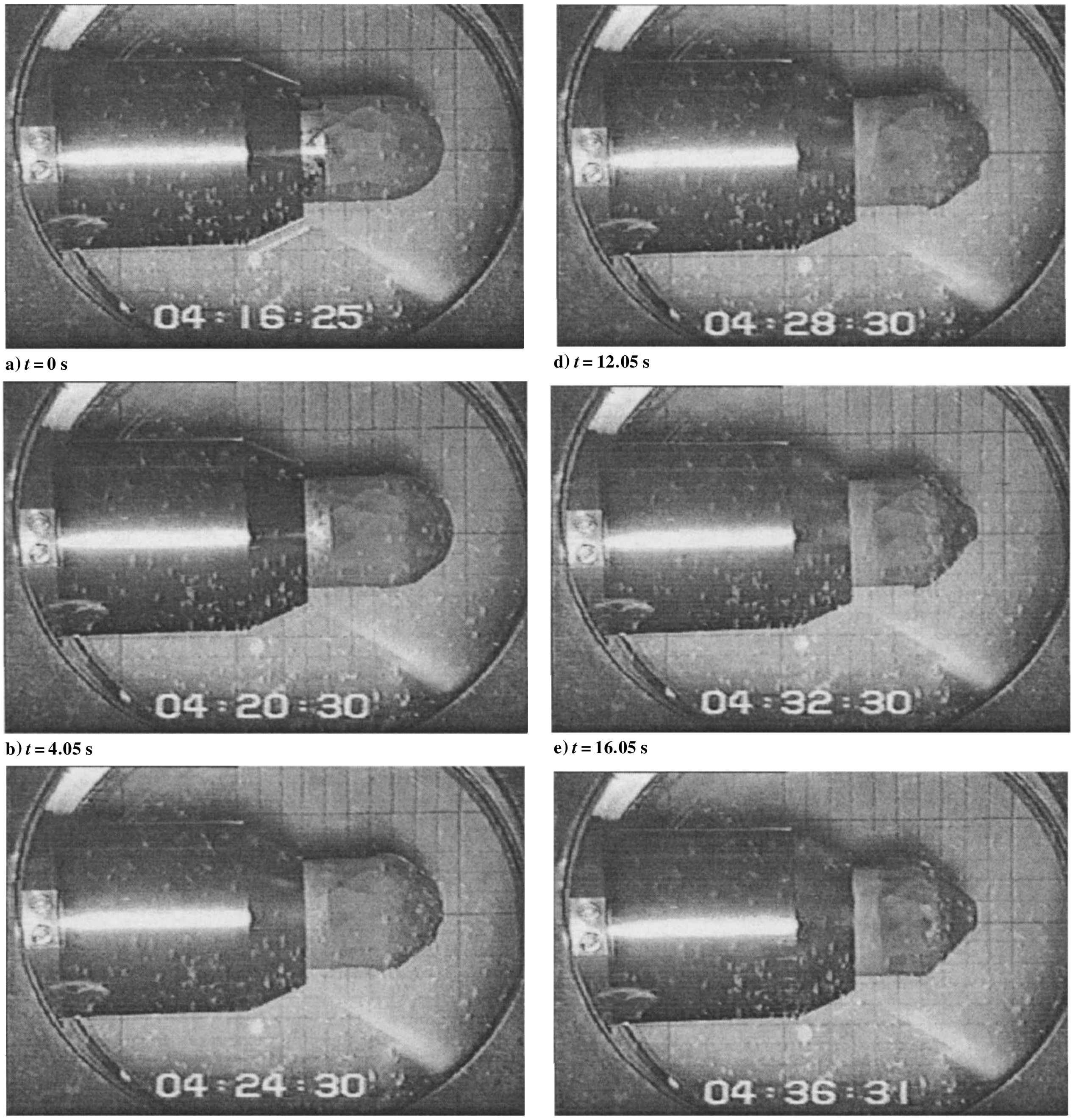

a) $t = 0$ s

b) $t = 4.05$ s

c) $t = 8.05$ s

d) $t = 12.05$ s

e) $t = 16.05$ s

f) $t = 20.06$ s

Fig. 6 Time-lapse photographs of baseline case 1 from initial removal of shielding ($t = 0$ s) through end of run ($t = 20$ s); time after removal of shielding is indicated under each picture.

points after the onset of ablation. The scatter present corresponds to errors in reading the exact pixel location corresponding to the stagnation point. The slight apparent negative ablation at early times ($t < 5$ s) was believed to be due only to the data analysis being done by hand and not to any physical phenomena. Differences in the shield removal time after tunnel start did not appear to have effected ablation onset time or ablation rate as there was good agreement between the three runs.

The line slopes (recession rates) of the stagnation point for each run were determined using data points from the estimated time at which melting began (4 s) and later. The recession rates were consistent between runs (within 3%) as can be seen from the three least square fit lines on Fig. 7 and the actual recession rates (Table 1), but the recession rates had an experimental uncertainty of approximately 15%, based on scatter. The average recession rate at the stagnation point was 0.294 mm/s. The time at which melting began for each run was then calculated using interpolation back to the time of zero displacement. These ablation onset times could be determined to within approximately 0.5 s.

Deep-Cavity Model

Three separate wind-tunnel runs were conducted for the $L/D = 2.0$, deep-cavity models to assess repeatability and to vary the lip radius. With a deep cavity in the model, visual ablation began at the most forward point on the lip of the model. Figures 8a–8f show time-lapse images from run 3 (rounded lip). Note the jaggedness of the cavity lip as it began to ablate and that ablation did not remain symmetric throughout the run. Again, this could be due to inconsistencies in the ice model. Also note that ice was still present over the entire interior of the cavity at the conclusion of the runs, which suggested very little heating at the cavity base. Also visible in the

Table 1 Experimental recession rates and ablation onset times[a,b]

	Run 1		Run 2		Run 3	
L/D	Rate	Time	Rate	Time	Rate	Time
0	0.289	4.8	0.297	5.4	0.295	4.4
2.0	0.413	1.6	0.464	1.1	0.460	4.2

[a] Recession rates (rate) are in millimeters per second.
[b] Ablation onset times (time) are in seconds.

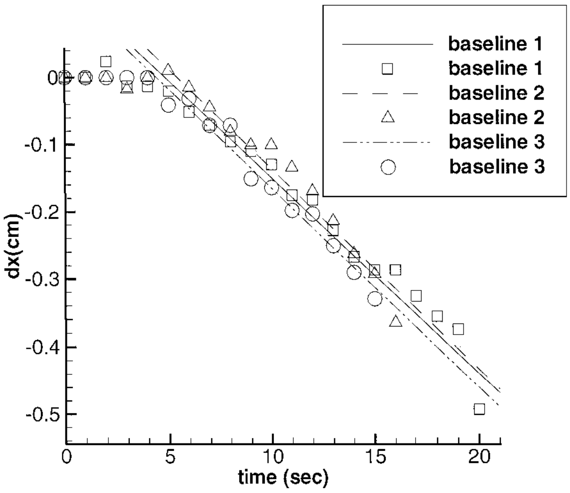

Fig. 7 Stagnation point position vs time for three repeated baseline cases.

video were hints of shock motion confirming that shock oscillations were present.

Because of the jaggedness of the cavity lip, an average lip position was used to compare the runs. The change in this average position over time is shown in Fig. 9. Note that in run 1 the model had a sharp cavity lip, whereas in runs 2 and 3, the cavity lip was rounded (~ 1 mm). Agreement between runs was not as good as for the baseline case both in terms of the recession rate and the time of ablation onset (Table 1). This is most likely due to the geometrical differences, that is, cavity lip radius, between runs. The differences could also be due to the shielding coming off in an irregular manner, the fibers at the cavity lip interfering with the ablation, an uncertain initial model temperature, the model being at a slight angle of attack, or defects in the model. However, one would think that these potential sources of discrepancy would apply to the baseline runs, too, but they were self-consistent.

A least-square linear fit of the position data was again used to obtain the average recession rate of each run. The recession rates appeared roughly constant over time (Fig. 9). The average recession rate for all three $L/D = 2.0$ cavity runs was approximately 0.445 mm/s, nearly twice as fast as for the baseline blunt model. Again, the recession rates are known within 15%. The onset of ablation appeared to occur at approximately 1–2 s, except in run 3 where ablation onset was delayed to 4 s. As for the baseline case, the ablation onset times are known within 0.5 s. The rounded lip in run 3 was formed using the drill press, whereas the rounding of the lip in run 2 was done entirely by hand (see Experimental Methodology, Models). It is, therefore, likely that the lip in run 3 was more uniformly rounded, which may have been a cause for the delayed ablation onset. The sharp-lip model in run 1 began ablating rapidly after about 1 s. This would be expected, as the heating near the lip should be severe.[1,2]

Shallow-Cavity Models

One wind-tunnel run was conducted for each shallow-cavity model ($L/D = 0.25$, 0.5, and 1.0) to determine trends. All three cases had sharp cavity lips.

The ice leading-edge positions vs time are seen in Fig. 10. The three shallow cavity models showed interesting trends. Although the different models appear to start ablating at approximately the same time and rate, the rates begin to differ a few seconds into the run. The shallowest cavity's ($L/D = 0.25$) recession rate appears to slow down first at about $t = 9$ s, whereas the $L/D = 0.5$ rate slows down later ($\sim t = 15$ s), and the $L/D = 1.0$ case does not appear to slow its recession rate at all. The change in recession rate appears to be correlated with the time at which the cavity has completely ablated away. That is, the $L/D = 0.25$ cavity was 0.3 cm deep, whereas the $L/D = 0.5$ cm cavity was 0.6 cm deep.

Summary

As expected, introducing a forward-facing cavity into the nose tip of a projectile did change the ablation rate. Although deeper cavities seem to have slower ablation rates than shallower cavities, the ablation rate of the stagnation point of the baseline case is nearly two times slower yet. The onset of ablation also appeared to occur later for the stagnation point of the baseline case than for any of the cavity cases, but was very close to the time of the blunt-lip, $L/D = 2.0$ run (case 3). The hoped for delay in the ablation onset may not have been observed due to the utilization of an insufficiently deep cavity in this experiment or because the cavity lips were not sufficiently rounded.

The effect of cavity depth only is illustrated by Fig. 10, which includes the sharp-lip, deep-cavity case along with the shallower sharp-lip cavity cases. The sharp-lip, deep-cavity case appears to agree better with the other sharp-lip cases than with the other deep-cavity cases. Therefore, it is thought that lip radius has a strong effect on ablation. In fact, Engblom[1] found, and it is shown in detail hereafter, that rounding the lip was necessary to reduce the local mean surface heating because the airflow into the cavity directly impinges on the cavity lip. Based on these findings, it is believed that there is an optimum lip radius at which heating will be minimized subject to other constraints. It is possible that a highly blunted lip will cause the greatest delay in the onset of ablation.

Numerical Results

The present numerical findings will be separated into three sections: a baseline case, an infinitely sharp-lip cavity case, and a rounded-lip cavity case.

Baseline

A single-zone grid was generated for the baseline (no cavity) flowfield computations (Fig. 11). To ensure convergence of the calculated surface heat flux distributions, a grid refinement study was conducted. Surface heat flux distributions for four grids were obtained for a steady flowfield around the baseline body. Each grid contained 120 points along the surface body, which was fully adequate to resolve the flowfield. The grid fineness near the wall (i.e., surface cell thickness $dx_{\min}$ and the number of grid cells near the wall) was varied for the four grids from $dx_{\min} = 1.27 \times 10^{-3}$ to 1.0×10^{-4} mm. The coarsest grid ($dx_{\min} = 1.27 \times 10^{-3}$ mm) was calculated using a flux limiter coefficient based on pressure of 5, whereas the three finer grids were calculated using a flux limiter coefficient of 10. The grids studied contained 120, 140, 160, and 180 cells normal to the wall, respectively (each finer grid had more normal cells). Surface heat flux distributions for each of the four grids are shown in Fig. 12.

Although complete grid convergence was not found between any two grids, there is less than a 1% difference between the two finest grids ($dx_{\min} = 2.5 \times 10^{-4}$ and 1.0×10^{-4} mm). Because the abrupt increase in surface heat flux that was observed with the first grid refinement does not occur with further refinement, the grid is considered adequately converged with a minimum surface spacing of $dx_{\min} = 2.5 \times 10^{-4}$ mm. Also, note that the best agreement with the Fay and Riddell[19] value for peak heating at the nose (in these cold, high-speed flows) of 268 kW/m^2 occurs with the coarsest grid and disagrees with the finer grid results by 3–4%.

The spatially converged grid ($dx_{\min} = 2.5 \times 10^{-4}$ mm) was used to obtain the surface heat flux distribution $q(x, y)$ and adiabatic wall temperature distribution $T_{aw}(x, y)$ with 200 cells along and 160 cells

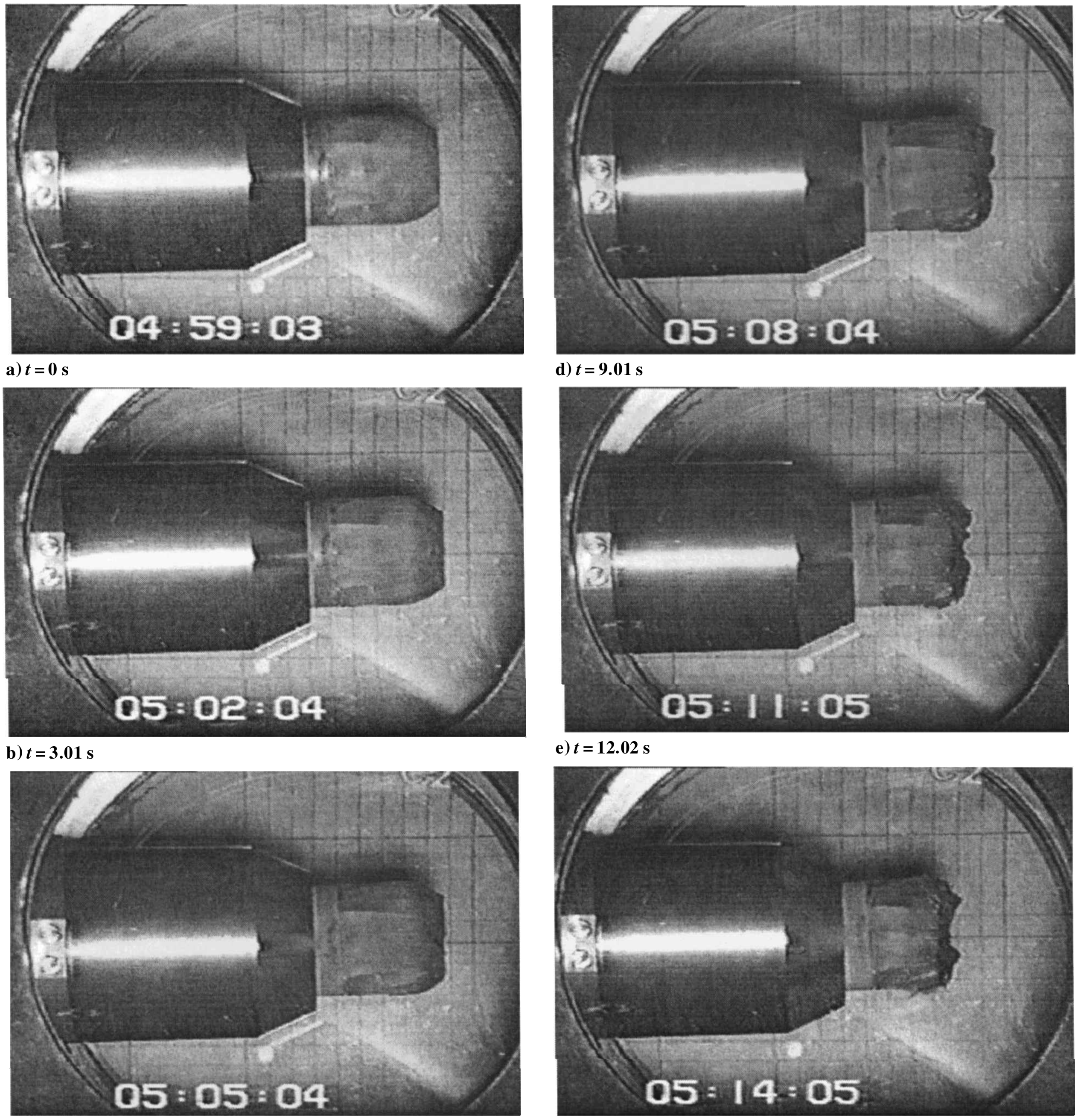

a) $t = 0$ s

b) $t = 3.01$ s

c) $t = 6.01$ s

d) $t = 9.01$ s

e) $t = 12.02$ s

f) $t = 15.02$ s

Fig. 8 Time-lapse photographs of $L/D = 2.0$ cavity case, run 3, from initial removal of shielding ($t = 0$ s) through end of run ($t = 15$ s); time after removal of shielding indicated under image.

normal to the body surface. A greater number of cells along the body surface were used to obtain the distributions to aid in transferring the data to the heat conduction code.

A single zone grid containing 27,600 nodes and 27,300 elements (shown later) was utilized for the heat conduction calculations. A brief study, conducted to determine the effect of dt_i, showed little difference in ablation onset time (less than 0.5%) regardless of dt_i. At early times ($t < 0.75$ s and $T_{\max} < 200$ K), when thermal gradients were greatest, times to reach a given temperature never differed by more than 0.004 s between $dt_i = 0.02$ and 0.01 s. Therefore, $dt_i = 0.02$ s was utilized.

Using the $h(x, y)$ calculated from the flowfield solution and $dt_i = 0.02$ s, the time to ablation onset at the stagnation point was 3.7 s (Fig. 13). This is within 25% of the average experimental time to ablation onset (4.9 s). In fact, compared to the shortest experimental ablation onset time (4.4 s), the computational result is within 15%. Either way the computational results are quite reasonable.

Note that the increase in temperature was initially quite fast (as indicated by the initial large slope of the curve in Fig. 13) and then slowed down as the forward portion of the body heats, that is, the heat flux to the surface decreases because the temperature difference at the surface decreases. Additionally, the temperature increase for the simulation was mostly confined to the forward quarter of the body (Fig. 14). The temperature gradients are large at the forward portion of the body and become smaller as the heat is conducted into the body. This is, of course, seen in the general one-dimensional heat transfer result, but is also affected by changes in thermal conductivity and specific heat as the body heats and the increased surface area over which the temperature rise must take place. There is very little temperature increase (~2 K) toward the right-hand side of the solid (where the experimental model was connected to a brass

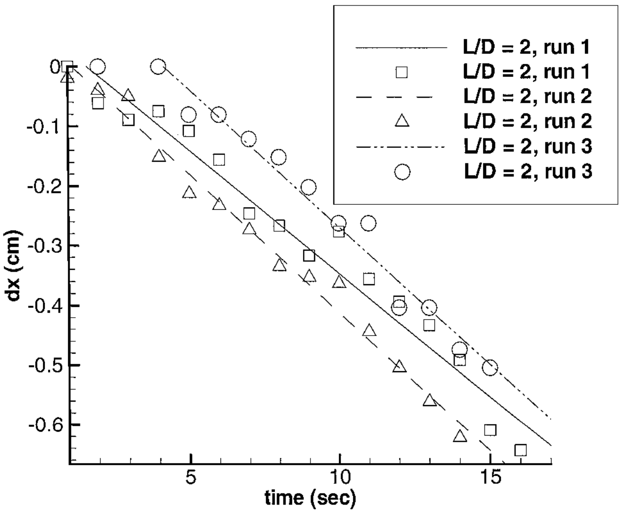

Fig. 9 Average nose-tip position vs time for $L/D = 2.0$ cavity cases; lines are least-square linear fits of the data points after the onset of ablation.

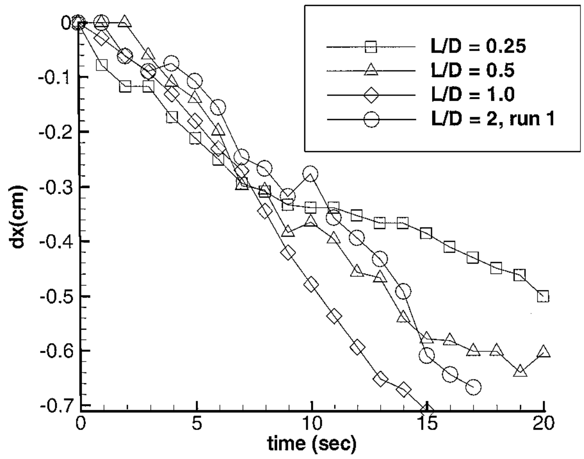

Fig. 10 Position vs time plots for the three shallow sharp lip cavity cases and the one deep, sharp-lip cavity case. (Note obvious changes in slope of data points at 6–9 s.)

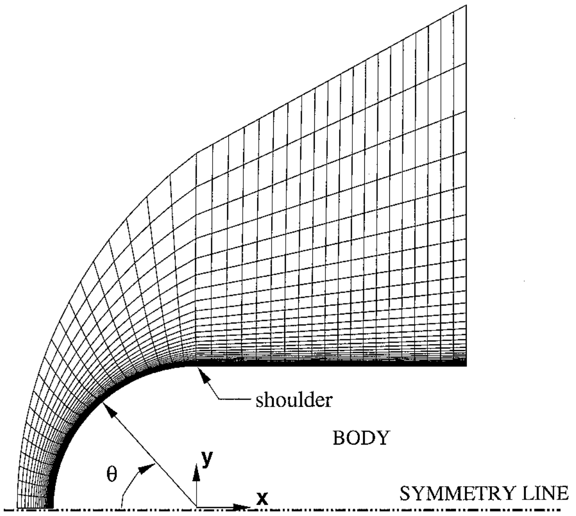

Fig. 11 Schematic of the single-zone flowfield grid used for baseline calculations.

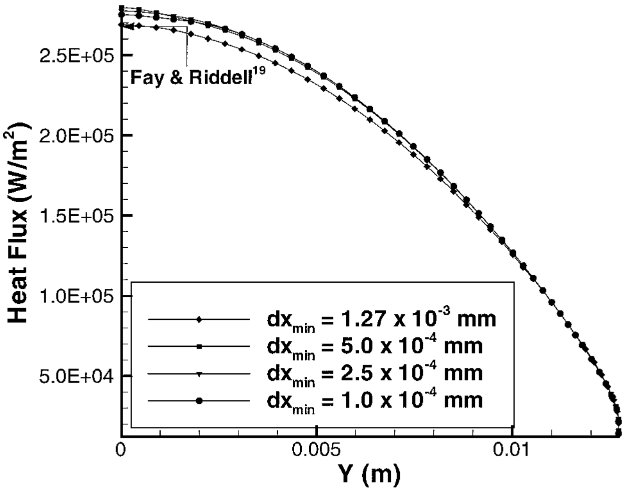

Fig. 12 Surface heat flux distribution over baseline blunt body on four different grids; surface grid fineness levels ($dx_{\min}$) as indicated, body was isothermal at 100 K.

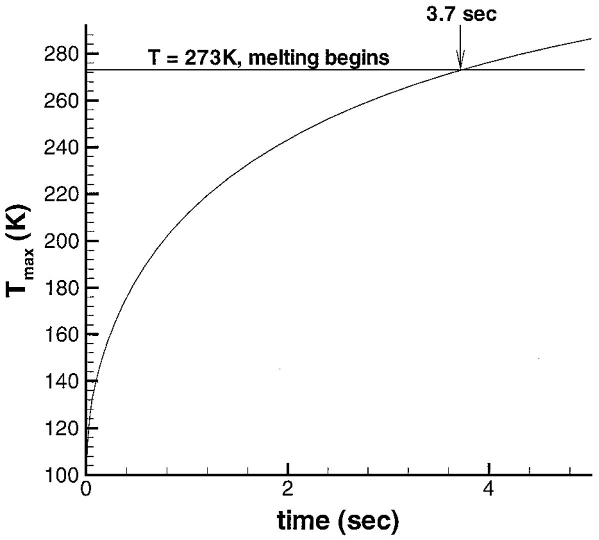

Fig. 13 Temperature history for baseline simulation at maxima (stagnation point).

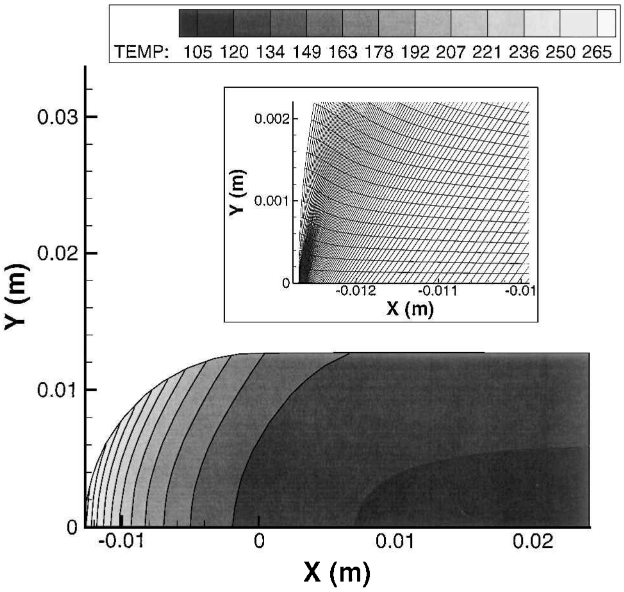

Fig. 14 Temperature contours of baseline simulation at 3.6 s, just prior to ablation onset; inset shows magnified view of the grid in the stagnation region.

mount) indicating that modeling only the pure ice nose tip should give reasonable results.

A grid resolution study for the solid body was conducted by halving the number of points on the solid-body surface. The coarser grid contained only 6925 nodes and 6775 elements. The difference between time to onset of ablation for the two grids was approximately 0.01 s (a 0.3% error). Therefore, the finer grid should more than adequately resolve the problem.

Infinitely Sharp-Lip Cavity

A two-zone grid (Fig. 15) was used for the sharp-lip cavity flowfield computations where one zone encompassed only the cavity. The flowfield computation was first performed using a coarse grid ($dx_{\min} = 1.0 \times 10^{-3}$ mm) and 1000 time steps per cycle until a pseudosteady oscillating solution was reached. The simulation was considered pseudosteady once the mean surface heat flux distribution and base pressure level did not change appreciably for several consecutive cycles. A portion of the pressure history at the base of the cavity is presented in Fig. 16. The oscillations were self-sustained at about 3 kHz for this cavity geometry, as expected.[4]

An extensive temporal and spatial resolution parameter study (isothermal wall boundary condition of 100 K) was then conducted to confirm that the heat flux was indeed converged. First, mean heat flux distributions for one pressure cycle were computed for various numbers of time steps per cycle. Results of this study for the outer portion of the body (Fig. 17) showed reasonable temporal convergence when 4000 time steps per cycle (six subiterations per time step) were used, although 3000 or even 2000 would also have been adequate.

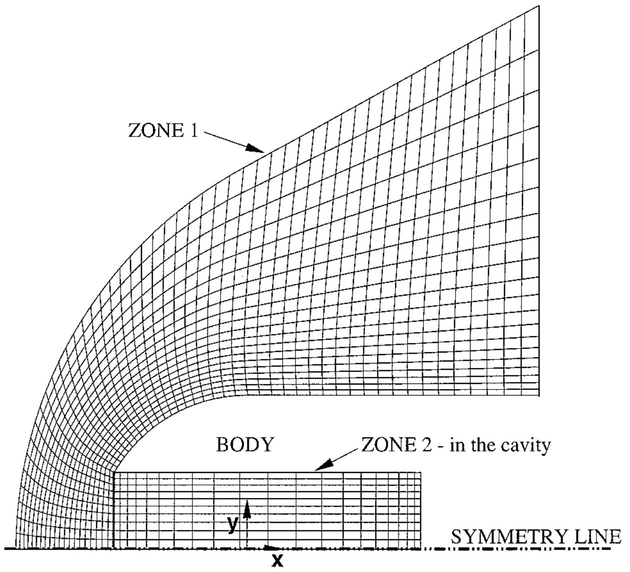

Fig. 15 Schematic of the flowfield grid used for $L/D = 2.0$ sharp-lip calculations.

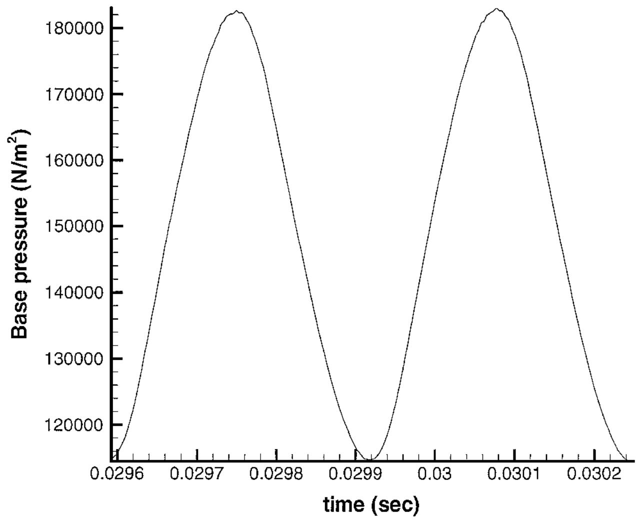

Fig. 16 Portion of base pressure history for sharp-lip cavity.

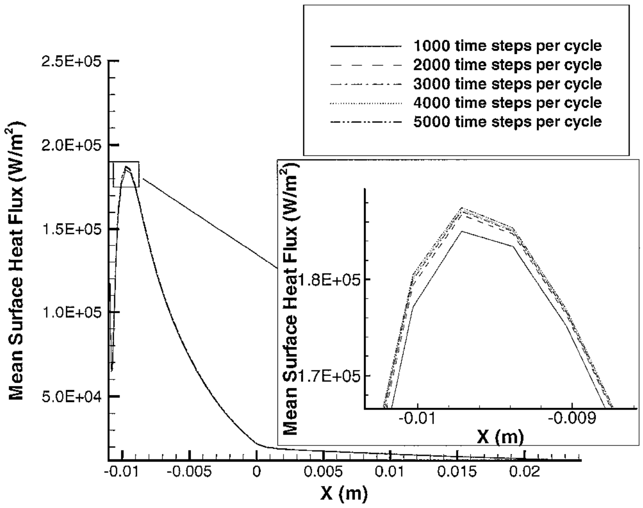

Fig. 17 Mean heat flux distribution on outside of body for various numbers of time steps per cycle to determine temporal convergence (six subiterations per time step).

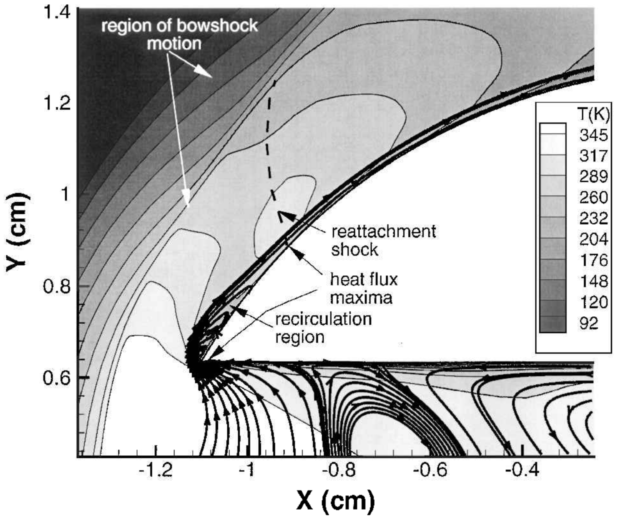

Fig. 18 Mean temperature contours with select streamlines in the vicinity of the sharp lip. (Note that, because the flow is highly oscillatory, major flow features such as the bow shock, the separated recirculation region, and the reattachment shock are blurred by the motion.)

Spatial resolution was then verified using 4000 time steps per cycle and by an increase in grid fineness along the wall. Of the five grids studied, four contained 300 cells along the outer surface body and 399 cells normal to the wall; the fifth and coarsest grid contained 100 points in each direction. To resolve the cavity adequately, the coarsest grid contained 140 cells normal to the line of symmetry and 45 cells from the cavity basewall to the cavity lip. The four other grids contained 200 cells normal to the line of symmetry and 99 cells from the cavity basewall to the cavity lip.

The surface cell spacing was varied for the five grids studied from 1.0×10^{-3} mm (coarse cell distribution) to 1.0×10^{-4} mm. As resolution near the wall was increased, there was an increase in the number of small heat flux fluctuations on the outer lip (most likely due to the solution capturing a greater number of small lip eddies). To work around this phenomenon, and keep computational times reasonable, the area around the reattachment shock (Fig. 18), where a second, smaller, peak in heating occurs, was more closely examined. Comparing the mean surface heat flux distributions at the wall (Fig. 19), a grid with $\mathrm{d}x_{\min} = 2.5 \times 10^{-4}$ mm was considered converged because there was very little difference between it and a grid with $\mathrm{d}x_{\min} = 5.0 \times 10^{-4}$ mm. If the spacing is reduced further to $\mathrm{d}x_{\min} = 1.0 \times 10^{-4}$ mm, still finer scale eddies appear right near the singularly sharp lip. These eddies do not appear to alter appreciably the high heating peak near the reattachment shock.

The spatially converged grid (300×399 cells outside, 200×99 cells in the cavity, and $\mathrm{d}x_{\min} = 2.5 \times 10^{-4}$ mm) with 4000 time steps per cycle was then used to determine the pseudosteady solution. The mean surface heat flux distribution was found to be adequately converged between the 98th and 99th cycle from the start of the calculations with most of the pressure oscillation cycles calculated at coarser temporal and spatial resolution.

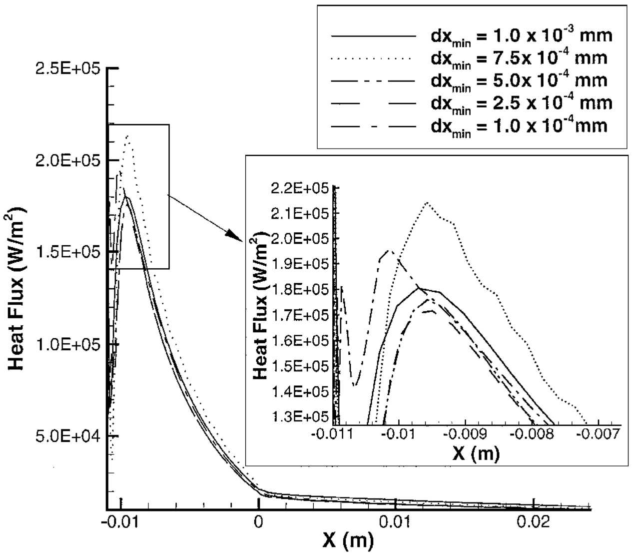

Fig. 19 Mean heat flux distribution on outside of body for various surface spacings to determine grid convergence.

Starting at the cavity base at the centerline, Fig. 20c shows that there is very low mean surface heat flux along the cavity basewall. The mean heat flux then increases along the length of the cavity to reach a peak value ($\sim 425{,}000$ W/m^2) near the sharp lip at $x = -0.011$ m (Fig. 20b). The mean heat flux again decreases along the outside of the body before the separation region, increases through the recirculation region to a local maximum at the reattachment shock ($-0.0105 \lesssim x \lesssim -0.0095$ m), decreases rapidly to the shoulder of the body ($-0.0095 \lesssim x < 0$ m), and finally tapers off to negligible heat flux at the end of the nose tip model ($x > 0$ m) (Fig. 20a). These mean surface heat flux features were expected.[1,20]

The nodal distribution on the body surface from the flowfield calculation grid was used to create the grid for the solid-body heat conduction calculations. This grid contained 49,135 nodes and 48,135 elements. The resulting grid (close-up in inset, Fig. 21) was probably overresolved based on the results of the baseline solid-body grid resolution study. Additionally, the spacing needed to adequately resolve solid-body heating is much larger than that needed to adequately resolve a hypersonic boundary layer. As computational time was not an issue for this case, a grid containing fewer, larger elements was not created. The effect of the choice of time step $\mathrm{d}t_i$ was investigated. There was very little difference in ablation onset time (less than 0.6%) regardless of $\mathrm{d}t_i$ and $\mathrm{d}t_i = 0.01$ s was utilized.

The time to ablation onset, which occurred at the sharp cavity lip, was 1.4 s. The simulation predicted a time to ablation onset within 13% of the experimental time to onset of ablation (1.6 s for $L/D = 2.0$, run 1). Although this appears to be a large percentage difference, the actual time difference was small (0.2 s). Because of the way in which experimental data were analyzed (1-s intervals), exact ablation onset was not seen. Instead, ablation onset was

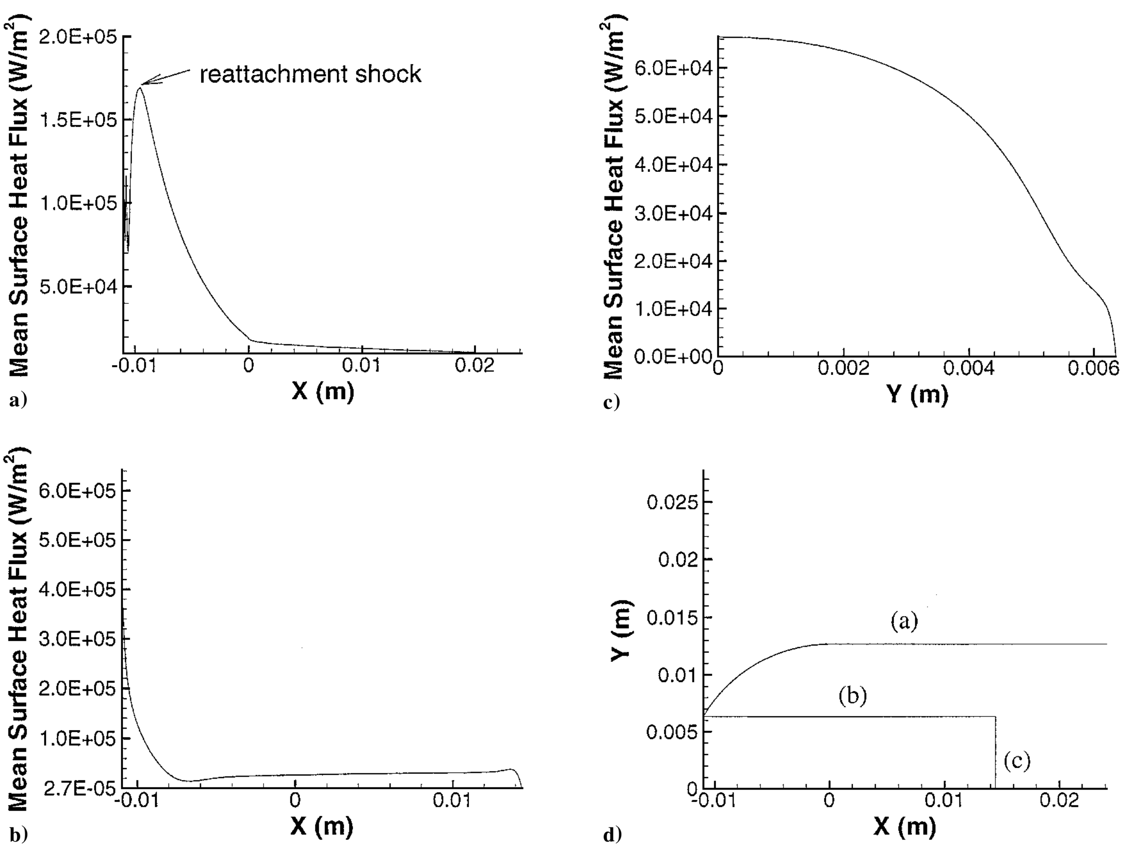

Fig. 20 Mean heat flux distribution for isothermal wall at 100 K along a) outside of body, b) cavity top wall, and c) cavity base wall; d) schematic of body.

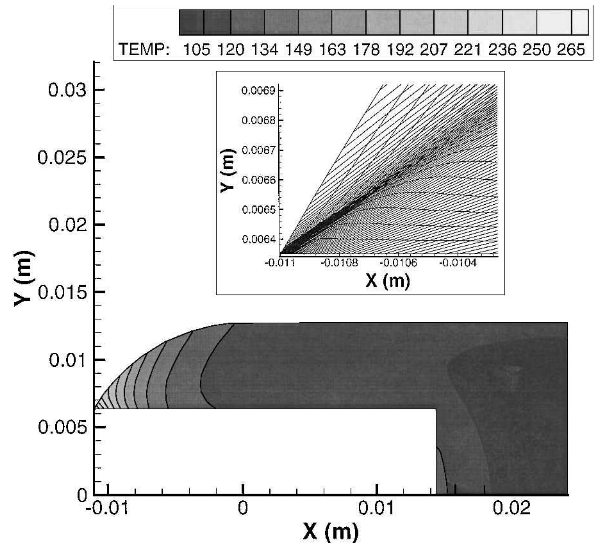

Fig. 21 Temperature contours of sharp-lip cavity simulation at 1.3 s, just prior to ablation onset; inset shows magnified view of grid in the lip region.

interpolated from the ensuing recession rate (assumed linear). This could account for the difference in ablation onset time. Additionally, the computations were for an infinitely sharp-lip cavity, whereas the experimental cavity would have had an finite lip radius, however small. Therefore, a higher heat flux, and, hence, a quicker ablation onset time was expected computationally.

The high heat flux at the sharp lip of the cavity (Fig. 20) was conducted away from the lip and through the body. The high heat flux at the lip caused a greater temperature increase with time in the lip region than in the remainder of the solid body (Fig. 21). However, only a very small portion of the body (front one-fourth of the cavity) experiences a temperature increase of any significance. The remainder of the nose remains cold, which suggests that the metal support structure used in the experiment did not significantly influence the heat transfer problem.

Rounded-Lip Cavity

A separate temporal resolution study was not conducted for the rounded-lip cavity case because it was assumed that the sharp-lip case, for which such a study was performed, was the more temporally rigorous case. Therefore, the resulting temporal resolution should be conservative for the rounded-lip geometry.

A separate spatial resolution study of the unsteady fluid mechanics for the rounded-lip cavity case verified that the grid spacing used for the sharp-lip cavity flowfield was again adequate to capture the flowfield physics. Using approximately 4000 time steps per cycle (six subiterations per time step), time-averaged (mean) heat flux distributions obtained on grids with surface cell spacings of 2.5×10^{-4} and 5.0×10^{-5} mm were compared. Each grid was composed of five zones (Fig. 22) to maintain grid quality and resolution near the lip and shock regions. The zones were chosen such that the bow shock would not cross the zone boundaries, but would remain fairly well aligned with the grid. One zone encompassed only the area around the lip (zone 3). A second zone (zone 4) was used to extend this area to the outflow boundary. Zones 1, 2, and 5 contained the cavity and the remainder of the flowfield.

Differences in the mean heat flux distributions due to surface cell thickness (Fig. 23) were mostly confined to the base of the cavity. Although these differences appear large (~ 14%) at the base of the cavity (Fig. 23a), the total magnitude was very low. This difference is likely caused by the mean flow circulation within the cavity not being periodic (Fig. 24), which would cause small changes in the cavity base wall mean heat flux from cycle to cycle. Near the lip, the mean heat flux for two sequential pressure oscillation cycles on the fine grid bound the average mean heat flux for the medium grid (Fig. 23b), which suggested that the average mean heat flux value for the fine grid would be very similar to that for the medium grid. In fact, the average mean heat fluxes for the two grids differ by approximately 0.1% at their maxima. Therefore, a grid with $dx_{\min} = 2.5 \times 10^{-4}$ mm (zone 1, 259×99; zone 2, 74×199; zone 3, 49×379; zone 4, 40×49; and zone 5, 74×35) was used to determine the mean heat flux distribution and the mean adiabatic wall temperature distribution.

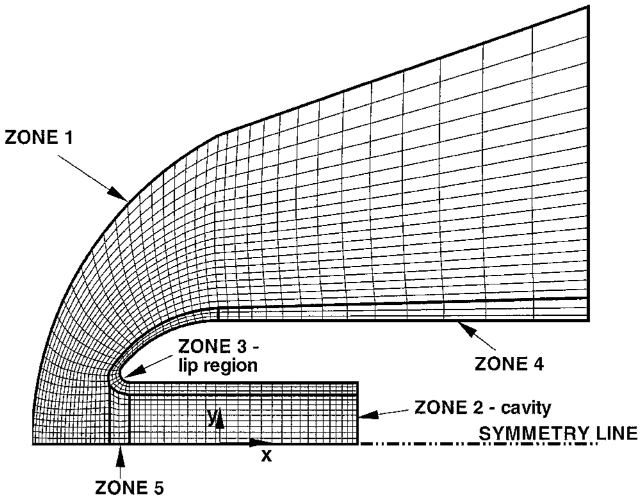

Fig. 22 Schematic of the flowfield grid used for *L*/*D* = 2.0 rounded-lip calculations.

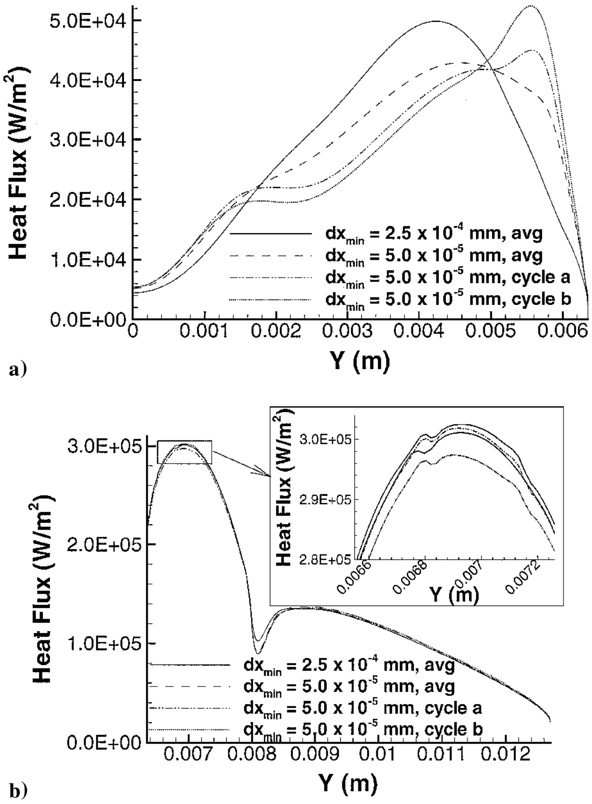

Fig. 23 Mean heat flux distribution a) at base of cavity and b) in the lip region and on outside of the body for two different surface spacings.

The pressure oscillations, and changes in relative Mach number, caused temperature fluctuations within the cavity. Most noticeable was an increase in mean heat flux off the centerline at the cavity base wall, caused by the circulation patterns within the cavity (Fig. 24). Additionally, a cold finger of gas remained on the centerline at the cavity base wall, which accounted for the negligible mean heat flux here. To account for small, noncyclic fluctuations (< 1%) in the mean

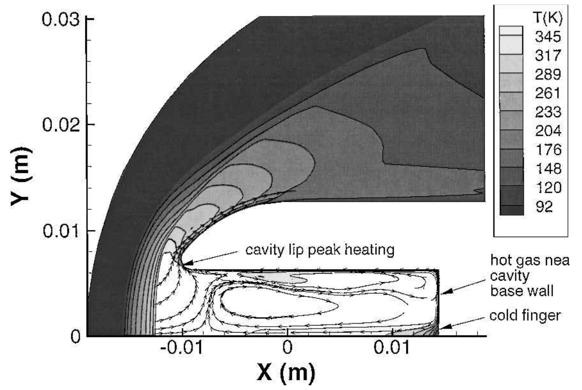

Fig. 24 Mean temperature contours for rounded-cavity lip flowfield; note that the bow shock is smeared by time averaging.

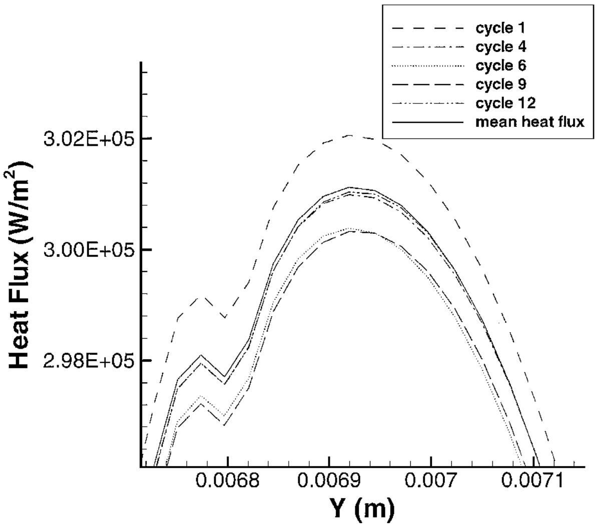

Fig. 25 Mean heat flux distribution at cavity lip for 5 of the 13 consecutive cycles that were averaged; the solid line represents the mean heat flux averaged over 13 cycles.

heat flux in the lip region (Fig. 25), the mean heat flux was averaged over 13 cycles (pressure oscillation cycles 186–198). The average mean heat flux (Fig. 26) was then used to calculate $h(x, y)$. The reference temperature distribution $T_{\mathrm{aw}}(x, y)$ was determined on the same grid after 140 pressure oscillation cycles.

The grid for the solid body was constructed using the nodal point distribution on the body surface from the flowfield grid (close-up in inset, Fig. 27). This resulted in a 31,133-node, 30,733-element grid that was believed to more than adequately resolve the solid-body heating for the same reasons as for the sharp-lip cavity case. Therefore, no grid resolution study has been performed. A time resolution study was performed with convergence easily obtained with $\mathrm{d}t_i = 0.02$ s.

The resulting time to onset of ablation was 2.5 s. The peak temperature occurred at the lip center, as indicated in Fig. 27. It appears that, for this case, the experimental ablation onset time of 4.2 s ($L/D = 2.0$, run 3) was not well predicted (a 40% difference from the computational result). Despite this relatively large difference, the simulation was still believed to have returned a result that was reasonably consistent with the experiments for several reasons. First, the exact experimental lip shape was unknown, and the initial ice temperature was only an estimate. It is also true that we are not able experimentally to see exactly this point of computational ablation onset. Therefore, ablation may have begun earlier on in the experiment than was visually apparent. Additionally, as with the sharp-lip cavity case, the experimental ablation onset time was interpolated from the ensuing recession rate. Because of the scatter of the data, the ablation onset time could have been off by as much as 1 s. Finally, in the computations, iterating between the flowfield and the solid-body heat conduction codes may be required due to changes in the wall temperature distribution having an effect on the flowfield physics and, hence, $h(x, y)$.

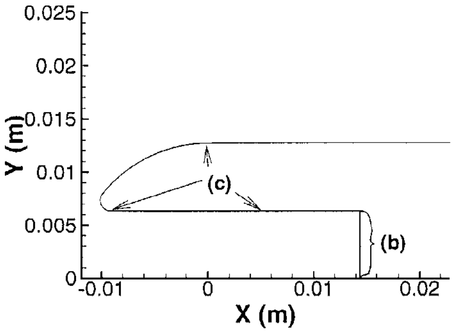

Fig. 26a Schematic of body.

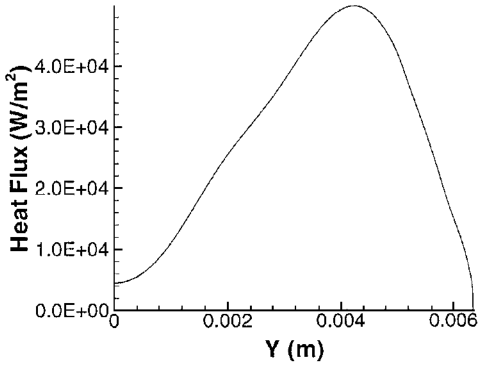

Fig. 26b Mean heat flux distribution averaged over 13 cycles for isothermal wall at 100 K along cavity base wall.

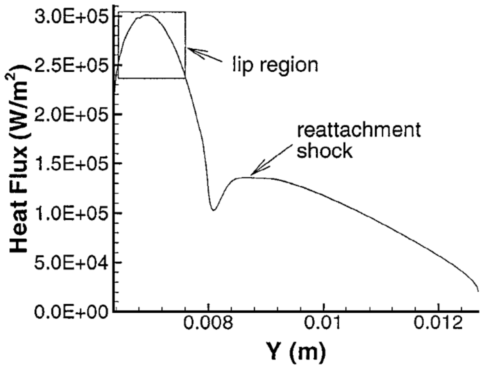

Fig. 26c Mean heat flux distribution averaged over 13 cycles for isothermal wall at 100 K along cavity lip and outside of body.

The temperature rise within the solid body (Fig. 27) was consistent with the mean flowfield temperatures (Fig. 24) as well as the average mean heat flux distribution. The high-temperature areas in the flowfield correspond to higher heat fluxes and, hence, a faster increase in the solid-body temperatures.

Turbulence Model

The bow shock oscillations cause the surface heat flux to vary over one oscillation cycle. The surface heat flux is lowest during the cavity outflow portion of the cycle despite the increased relative Mach number across the forward-moving shock because the hot gas is convected away from the body. During the cavity inflow portion of the cycle, when the relative Mach number and, hence, temperatures behind the shock are lower, surface heat flux is actually greatest due to the existence of a stagnation point on the blunted lip. Because a stagnation point still exists on the blunted lip, transition may occur.

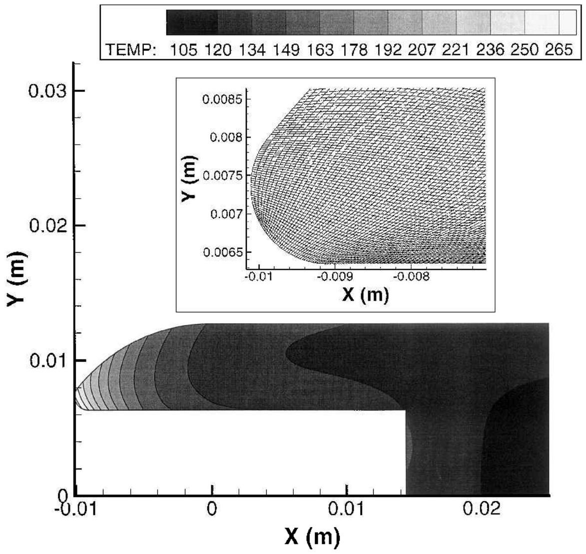

Fig. 27 Temperature contours of rounded lip cavity simulation at 2.4 s, just prior to ablation onset; inset shows magnified view of grid in the lip region.

The sonic line, after which transition appears to have occurred on the blunt body, was downstream of the rounded cavity lip during peak heating. Therefore, if the fluid dynamics of the cavity lip and the blunt body are similar, the position of the sonic line indicates that transition would not take place in an area of peak heating. Unfortunately, experimental verification of whether or not transition occurred was not obtainable. Therefore, a numerical method was investigated to determine if turbulent heating was important or if the flow could continue to be modeled as laminar.

To do this, a mean heat flux distribution using the k–ε turbulence model was obtained by use of the same flowfield grid as for the laminar case. Unfortunately, it was found that approximately 16,000 time steps per cycle with 18 subiterations were needed to accurately resolve this simulation in time. The time requirement for this temporal accuracy (59 Cray T90 h per cycle) is nearly prohibitive. Hence, confirmation of a truly pseudosteady solution (each cycle being periodic and having the same mean heat flux) was not obtained, and so the current solution is, for now, being treated as if it were pseudosteady. The heat flux at the base of the cavity for the turbulent case was found to be 270% greater than the laminar case, whereas the peak heat flux at the cavity lip (473 kW/m^2) was found to be only 50% greater. The accuracy of the heat flux at the base of the cavity cannot easily be determined as no experimental data were obtained in this area. However, the increased heat flux at the cavity lip over that of the laminar case produces a much earlier ablation onset time, 0.94 s, than was found assuming a laminar flowfield. This agrees to within 15% of the experimental ablation onset time for the $L/D = 2.0$, run 2 case (1.1 s). Therefore, it is possible that this lip configuration may indeed transition. However, it is currently unclear as to what may have caused the transition. Because the lip for the comparable experimental case was hand rounded, nonuniformity of the lip was possible (different lip radii, nicks, etc.), which would have caused transition as compared to the more uniformly rounded run 3, which, having a much longer ablation onset time, appears to have remained laminar. Because the laminar flowfield assumption appears reasonably valid for the comparison to the better made model and requires much less computational time, it will continue to be utilized in future computations.

Conclusions

The experimental method looks promising, although some of the results are unexpected. The shielding appears to adequately protect the ice model during wind-tunnel startup, though the temperature rise of the ice prior to exposure remains to be investigated. The mold appears versatile enough to accommodate a number of different geometries without much modification. Water ice seems to work well as a low temperature ablator; it could easily be formed to the desired shapes.

The results between the baseline no-cavity cases were consistent. The discrepancies between deep-cavity runs need to be investigated further. It remains unclear why ablation onset occurs earlier in the $L/D = 2$, round-lip case than the baseline case for what was thought to be a sufficiently deep cavity based on results by Engblom.[1] All of the sharp-lip cavity cases (both shallow and deep) appeared to have similar ablation onset times and initial ablation rates. The sharp lip is, therefore, believed to negate any beneficial effect of a deeper cavity. However, ablation onset seems to be delayed and ablation rates decreased with increased cavity lip radius for the deep-cavity case.

A numerical procedure has been developed to allow the flowfield and solid-body computations to be solved independently with linked boundary conditions. Most of the assumptions that were made for the flowfield calculations appear to have been reasonable except for, possibly, the assumption of laminar flow. Although numerical results appear reasonable based on experimental findings for the baseline no-cavity body where the stagnation point flow was probably laminar, the experimental results suggest that the flow is transitioning near (just after) the sonic line on this geometry.

Agreement between numerical and experimental ablation onset times is fairly good for both the baseline hemisphere–cylinder case and the sharp-lip cavity case. The agreement for the rounded-lip cavity case is not as good but is still promising because a number of variables still exist, including some experimental uncertainties. Whether or not $h(x, y)$ must be recalculated as the solid body warms in any or all of the three cases needs to be determined. Initial calculations using the k–ε turbulence model seem to validate the assumption of a laminar flowfield (at least for the cavity cases). This, in turn, suggests that the peak heating, which occurs on the lip during the inflow portion of the cycle, occurs while the flow on the lip is laminar. More generally, the use of the computational technique to predict the experimental flowfield physics of this complex, unsteady hypersonic flow problem appears to be working as expected. Obtaining more experimental data for which an ablation onset time has been more accurately determined would help to complete the benchmarking of the computations.

Acknowledgments

This work was supported in part by the U.S. Army Research Laboratory under Contract DAAA21-93-C-0101. The authors are grateful to William Engblom for many helpful technical discussions, to Scott Imlay and Moeljo Soetrisno, Amtec Engineering, for their technical support on INCA, and to Roy Hogan and W. Hugh Walker of Sandia National Laboratories for their help with COYOTE. Time was provided on the Cray J90 and SV1 by the University of Texas at Austin Texas Advanced Computing Center. The Cray T90 time was provided by U.S. Army Research Laboratory, Major Shared Resource Center. The authors would also like to thank James Sanders for all his time and help with the design and machining of the experimental setup.

References

[1] Engblom, W. A., "Numerical Investigation of Hypersonic Flow over a Forward-Facing Cavity," Ph.D. Dissertation, Dept. of Aerospace Engineering and Engineering Mechanics, Univ. of Texas, Austin, TX, Aug. 1996, pp. 20–29, 36, 41, 122–125, 128–143.

[2] Yuceil, B., "An Experimental Investigation of a Forward-Facing Nose Cavity on a Blunt Body at Mach 5," Ph.D. Dissertation, Dept. of Aerospace Engineering and Engineering Mechanics, Univ. of Texas, Austin, TX, Dec. 1995, pp. 77–94, 123–132.

[3] Yuceil, B., Dolling, D. S., and Wilson, D., "A preliminary Investigation of the Helmholtz Resonator Concept for Heat Flux Reduction," AIAA Paper 93-2742, July 1993.

[4] Engblom, W. A., Yuceil, B., Goldstein, D. B., and Dolling, D. S., "Experimental and Numerical Study of Hypersonic Forward-Facing Cavity Flow'," *Journal of Spacecraft and Rockets*, Vol. 33, No. 3, 1996, pp. 353–359.

[5] Engblom, W. A., Goldstein, D. B., Ladoon, D., and Schneider, S. P., "Fluid Dynamics of Hypersonic Forward-Facing Cavity Flow," *Journal of Spacecraft and Rockets*, Vol. 34, No. 4, 1997, pp. 437–444.

[6] Engblom, W. A., and Goldstein, D. B., "Nose-Tip Surface Heat Reduction Mechanism," *Journal of Thermophysics and Heat Transfer*, Vol. 10, No. 4, 1996, pp. 598–606.

[7] Farnsworth, S., and Wilson, D. E., "A Preliminary Investigation of the Helmholtz Resonator Concept for Heat Flux Reduction Part I: Experimental Program," Inst. for Advanced Technology, IAT.P 0024, Univ. of Texas, Austin, TX, Oct. 1992.

[8] Imlay, S. T., Roberts, D. W., Soetrisno, M., and Eberhardy, S., "INCA User's Manual," Ver. 2.5, Amtec Engineering, Bellevue, WA, May 1998.

[9] Steger, J. L., and Warming, R. F., "Flux Vector Splitting of the Inviscid Gasdynamic Equations with Applications to Finite-Difference Methods," *Journal of Computational Physics*, Vol. 40, No. 2, 1981, pp. 263–293.

[10] Gartling, D. K., and Hogan, R. E., "COYOTE—A Finite Element Computer Program for Nonlinear Heat Conduction Problems," Sandia National Lab., SAND94-1173, Albuquerque, NM, Oct. 1994.

[11] "GRIDALL User's Manual," Ver. 1.0, Amtec Engineering, Bellevue, WA, 1994.

[12] Blacker, T. D., "FASTQ Users Manual Version 1.2," Sandia National Labs., SAND88-1326, Albuquerque, NM, June 1988.

[13] Yuceil, B., and Dolling, D. S., "IR Imaging and Shock Visualization of Flow over a Blunt Body with a Nose Cavity," AIAA Paper 96-0232, Jan. 1996.

[14] Hobbs, P. V., *Ice Physics*, Clarendon, Oxford, 1974, p. 348.

[15] Johnson, V. J., *Properties of Materials at Low Temperature*, Pergamon, New York, 1961, p. 4.405.

[16] Childs, G. E., Ericks, L. J., and Powell, R. L., *Thermal Conductivity of Solids at Room Temperature and Below*, Cryogenics Div., Inst. for Basic Standards, National Bureau of Standards, Boulder, CO, Sept. 1973, p. 519.

[17] Reinecke, W. G., and Guillot, M. J., "Full Scale Ablation Testing of Candidate Hypervelocity Nose Tip Materials," *Proceedings of the 15th International Symposium on Ballistics*, Vol. 2, Secretariat 15th International Symposium on Ballistics, Tel Aviv, 1995, pp. 81–88.

[18] Reinecke, W. G., and Sherman, M., "Tip Survivability and Performance on Hypervelocity Projectiles," *Proceedings of the 14th International Symposium on Ballistics*, Vol. 1, American Defense Preparedness Association, Arlington, VA, 1993, pp. 575–586.

[19] Fay, J. A., and Riddell, F. R., "Theory of Stagnation Point Heat Transfer in Dissociated Air," *Journal of the Aeronautical Sciences*, Vol. 25, No. 2, 1958, pp. 73–97.

[20] Huebner, L. D., and Uteja, L. R., "Experimental Flowfield Measurements of a Nose Cavity Configuration," Society of Automotive Engineers, Paper 871880, Oct. 1987.